ARTICLE

Porous nitrogen and phosphorous dual doped graphene blocking layer for high performance Li–S batteries

Xingxing Gu[a,b], Chuan-jia Tong[c], Chao Lai [a], Jingxia Qiu[a], Xiaoxiao Huang[b], Wenlong Yang[b], Bo Wen[c], Li-min Liu*[c], Yanglong Hou*[b], Shanqing Zhang*[a]

Conductive confinement of sulfur and polysulfide via carbonaceous blocking layers can simultaneously address the low conductivity, volume expansion of sulfur during charge/discharge process and polysulfides shuttling effect in lithium–sulfur (Li–S) batteries. Herein, conductive and porous nitrogen and phosphorus dual doped graphene (p-NP-G) blocking layer is prepared via a thermal annealing and subsequent hydrothermal reaction route. The doping levels of N and P in p-NP-G measured by the X-ray photoelectron spectroscopy are ca. 4.38% and ca. 1.93 %, respectively. The dual doped blocking layer exhibits higher conductivity than N or P single doped blocking layer. More importantly, the density function theory (DFT) calculation demonstrates that P atoms and –P–O groups in the p-NP-G layer offer stronger adsorption to polysulfides than the N species. The electrochemical evaluation results illustrate that the p-NP-G blocking layer could deliver superior initial capacity (1158.3 mA h/g at the current density of 1 C), excellent rate capability (633.7 mA h/g at 2 C), and satisfactory cycling stability (ca. 0.09% capacity decay per cycle), which are better than the N or P single doped graphene. This work suggests that this synergetic combination of conductive and adsorptive confinement strategies induced by the multi-heteroatoms doping scheme is a promising approach for developing high performance Li–S batteries.

Introduction

The lithium–sulfur (Li–S) batteries have become one of the most attractive candidates that could surpass current lithium-ion batteries (LIBs) to achieve high charge capacity of 1675 mAh/g and energy density of 2500 Wh/kg and meet the demands of emerging electric vehicles[1, 2]. High natural abundance, low cost, and environmental-friendliness of sulfur bestows sulfur a promising raw material of cathode for Li–S rechargeable batteries[1, 3, 4]. However, commercialization of Li–S batteries is hindered by several barriers: (i) the insulating nature of elemental sulfur and intermediates Li_2S_2/Li_2S results in low utilization of the active materials[4, 5]; (ii) the dissolution of sulfur and intermediate polysulfides (Li_2S_x, $2<x\leq8$) into organic liquid electrolyte causes significant loss of the active mass and thus the passivation of the lithium anode, namely shuttling effect[5]; and (iii) the huge volume expansion (as high as 80%) of the electrode, which leads to the poor integrity and stability of the electrode[5]. In order to dissolve these obstacles, various strategies such as modifying the cathode, protecting the lithium anode and developing the new electrolyte and separator have been proposed[6]. Among them, the conductive confinement of sulfur and polysufides in a conductive porous carbon host is considered as the most promising strategy[1, 3, 7-9]. Recently carbonaceous materials, such as carbon nanoparticles[9], microporous carbon[10], multi-wall carbon nanotubes (MWCNTs)[11], carbonized biochar[12], carbonized paper[13], carbon/metal oxide composites[14], etc., applied as the polysulfides blocking layer in Li–S batteries have attracted increasing attentions because this approach can tackle the aforementioned barriers by remarkably enhancing the utilization percentage of the active materials and inhibiting the polysulfides from shuttling and consequently achieve high rate capability and extended cycling performance.

Graphene, due to its high electrical conductivity, superior mechanical flexibility, high chemical and thermal stability, high surface functionality, and extraordinarily large surface area[15, 16], is not only a good candidate as a high power and high energy electrode material in LIBs[15-19], but also a promising host for sulfur and polysulfides in Li–S batteries[5, 20-23]. Recently, heteroatoms, i.e., N, P, B, S, doped graphene exhibits enhanced electrochemical performance compared with the un-doped graphene in the fuel cells and LIBs[24-31]. It is believed that the
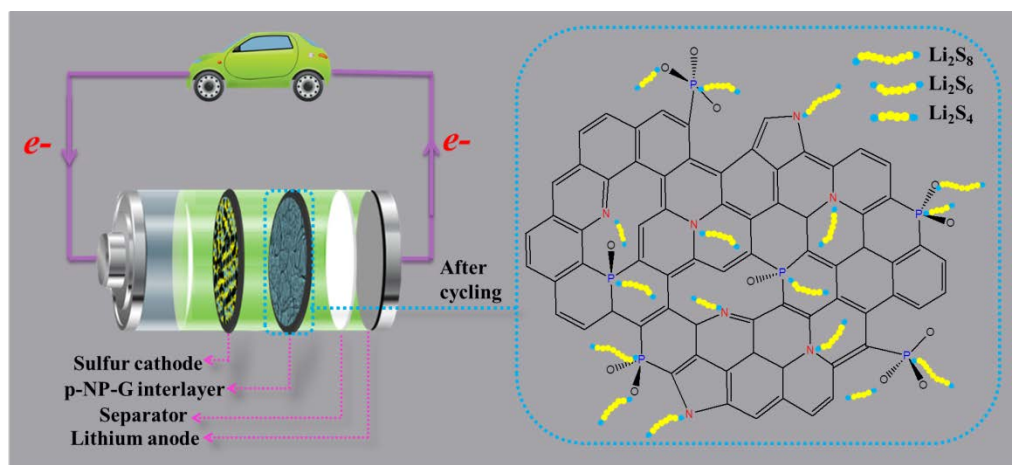
Scheme 1 A p-NP-G membrane incorporated in a Li–S battery and adsorptive mechanism of polysulfides at the p-NP-G membrane.

substantial improvement in performance is mainly attributed to the larger electronegativities of the doped atoms (e.g., N: 3.04, P: 2.19, B: 2.04, S: 2.58)[27, 29]. The doping of such atoms breaks the electroneutrality of the graphene and creates the charged sites, which is beneficial to the enhancement of electrochemical conductivity as well as adsorption capability. For instance, the P-doped graphene favors the adsorption of O_2 and therefore dramatically improve the electrochemical reduction of oxygen reduction reaction (ORR) process[27], while P- or N-doped graphene can improve the conductivity to facilitate the charge/discharge process in LIBs[25, 27]. Therefore, the heteroatoms doping has been extensively applied to boost electrochemical performances of Li–S batteries in order to improve the conductivity of the resulted graphene-based materials. For examples, the N-doped graphene/sulfur composites as the cathode materials in the Li–S batteries shows higher rate capability and specific capacity than the graphene/sulfur composite cathode due to the improvement of conductivity[32-34]. In addition, one research group has discovered that N and P dual doped graphene as anode for LIBs is superior to N or P single doped graphene in terms of conductivity improvement recently[30]. This is an excellent feature for application in Li–S batteries because this can address the low conductivity nature of sulfur and Li_2S_2/Li_2S. To the best of our knowledge, the applicability of such a material for Li–S batteries and the further functions of the dual doping have not been explored, and the application of the heteroatoms doped graphene as the interlayer in the Li–S batteries is still very limited[35].

In this work, in order to ensure high conductivity and effective retention of polysulfides in conductive confinement network, a porous N and P dual doped graphene (i.e., p-NP-G) nanomaterial is designed and synthesized. p-NP-G membrane is prepared with the p-NP-G powder and the polytetrafluoroethylene (PTFE) binder. The membrane is then used as a blocking layer to conductively confine sulfur and polysulfides in the cathode of Li–S batteries (as shown in the scheme 1). As expected, the Li–S battery with the p-NP-G blocking layer exhibits outstanding electrochemical performances in comparison with the Li–S batteries with the single doped graphene, i.e., the porous phosphorus doped graphene (p-P-G) and nitrogen doped graphene (p-N-G). The mechanisms corresponding to the outstanding electrochemical performances of the Li–S cells from the p-NP-G blocking layer have been investigated using extensive and systematic materials characterization, electrochemical evaluation and DFT theoretical simulation.

Experimental

Preparation and characterization

Synthesis of p-P-G: The graphite oxide (GO) was first prepared from the graphite powder by a modified Hummers method[26, 36]. In a typical experiment, 200 mg of GO was mixed with 1000 mg triphenylphosphine (TPP), 800 mg KOH and 200 ml ethanol. After the ethanol was evaporated, the mixture was annealed in a tube furnace at 800 °C under Ar atmosphere for 1 hour. After the furnace cooling to room temperature, the intermediate was collected and washed with 1 M HCl and distilled water to get the p-P-G material.

Synthesis p-NP-G: The p-NP-G was synthesized by hydrothermal reaction with ammonia solution as the nitrogen source. The synthesis steps are described as follows: 80 mg of p-P-G was dispersed in 10 ml distilled water by sonication, and then transferred into a 100 mL Teflon-lined autoclave with addition of ammonia solution (70 ml, 25 wt% in water). The autoclave was maintained at 200 °C for 12 hour, leading to production of black solids. Then 0.1 M HCl solution was used to remove the remaining ammonia solution. Distilled water and ethanol were used repeatedly to rinse the solid. The final product was collected by centrifugation and further dried in a vacuum oven at 60 °C overnight to get the p-NP-G material.

Synthesis of p-N-G: The synthesis method for the p-N-G is similar to prepare p-NP-G, but without addition of the phosphorus source (TPP) in the annealing process.

Fabrication of the doped graphene-coated separator: 13 mg

as-synthesized samples were separately dispersed in 5 ml NMP solution by sonicating for 30 minutes, and then 2 mg polyvinylidene fluoride (PVDF, used as binder) was added and stirred for 4 hours at ambient temperature. Using the Celgard 2300 separator as the filtering membrane, the vacuum filtration method was employed to get the large-size coated separator. After being dried in vacuum oven at 60 °C, the coated separator was tailored into many small wafers with a diameter of around 13 ± 0.2 mm. These small wafers, containing doped graphene of ca. 1.0 ± 0.1 mg/cm^2, act as both the separator and the blocking layer for the Li–S batteries.

Characterization of the materials

X-ray photoelectron spectroscopy (XPS) measurements were carried out on an Axis Ultra imaging photoelectron spectrometer (Kratos Analytical Ltd., Manchester, UK) using a monochromatized Al Kα anode, and the C *1s* peak at 284.8 eV was taken as an internal standard. X-ray diffraction (XRD) patterns were recorded on a Philips X'Pert Pro diffractometer (Philips Analytical, Almelo, The Netherlands) with Cu Kα radiation (λ= 1.5405 Å). Raman spectroscopy measurements were carried out on a Renishaw 1000 Raman imaging microscope system (Renishaw Inc, Illinois, USA) with an excitation wavelength of 514 nm. The Brunauer−Emmett−Teller (BET) method using nitrogen adsorption and desorption isotherms was performed on an ASAP 2020 system (Micromeritics, USA). The pore size distribution plot and pore volume were obtained by QSDFT method from the adsorption branch of the N$_2$ adsorption/desorption isotherms. The morphologies and the microstructures of the samples were examined using a HITACHI S-4800 (Japan) scanning electron microscopy (SEM) system and a FEI Tecnai F30 (USA) transmission electron microscopy (TEM), respectively.

Electrochemical measurements

Pure sulfur was mixed with carbon black and polytetrafluoroethylene PTFE in a weight ratio of 70: 20: 10 with ethanol as the dispersant. The resultant pastes were compressed on the Al foil by a tablet press, and then cut into discs with a diameter of 8.8 mm. Each wafer is approximately 0.5 cm^2 in area and 1.5 mg in average weight after dried in vacuum oven at 60 °C for 12 hours. The half-cells were assembled with home-made module in a glove box (M-Braun, Germany) under high pure Ar atmosphere. This configuration consists of the lithium metal as the counter electrode, and 1 M LITFSI in DOL/DME (1/1 v/v) containing 0.1 M LiNO$_3$ as the electrolyte. The calculation of the specific capacity is based on the mass of the sulfur active material. The charge and discharge performances of the half-cells were tested with the LAND CT-2001A instrument (Wuhan, China), and the potential range was controlled between 1.5 and 3.0 V at room temperature. The CHI 760E electrochemical workstation (CHI Instrument, Shanghai, China) was used to perform the cyclic voltammetry (CV) with a scan rate of 0.1 mV/s from 1.5 to 3.0 V. The electrochemical impedance spectroscopy (EIS) was also recorded using the same instrument over the frequency range from 100 kHz to 10 mHz. In addition, the current−voltage (*I−V*) curves were obtained on the CHI 760E using the compressed pellets of 8.8 mm in diameter, which were prepared

by rolling the doped graphene with the PTFE binder.

Computational validation

The density functional theory (DFT) calculations of structural relaxation and adsorption energy were calculated using the projector augmented wave method and implemented in the Vienna Ab Initio Simulation Package (VASP)[37-39]. The generalized gradient approximation (GGA) with the Perdew–Burke–Ernzerhof (PBE) functional[40] was used to treat the electron exchange correlation functional as in common graphene system[41]. To improve the description of long-range *van der Waals* interaction, we have employed the DFT-D3 method[42]. The cutoff energy of the projector augmented plane-wave basis set is 500 eV to ensure an accuracy of the energy of 1 meV per atom. Electronic minimization was performed with a tolerance of 10^{-5} eV. The k-point sampling uses the Monkhorst–Pack scheme on a 3×3×1 mesh.

Results and discussion

Materials characterizations

The as-prepared GO presented scaly appearance with grey colour, while all the heteroatoms doped graphene are black colour powder (as shown in Figure S1), which is caused by reduction of the GO in the annealing process[43]. As presented in XRD patterns in Figure 1, the peak at 2θ of 10.7° is a typical peak for the GO sample, indicating a layered structure with an interlayer spacing of 0.82 nm [31, 34]. After the annealing process at 800 °C, this peak completely disappeared, and a new well-defined peak at around 2θ of 26° appeared for the doped graphene, suggesting the successful reduction from GO to graphene with a perfect graphitic crystalline structure[31]. Moreover, a slight downshift of the 002 peak (2θ of 26°) is observed for p-NP-G as compared to the p-P-G or p-N-G, implying the interlayer spacing has been further increased due to the P and N dual doping[31].
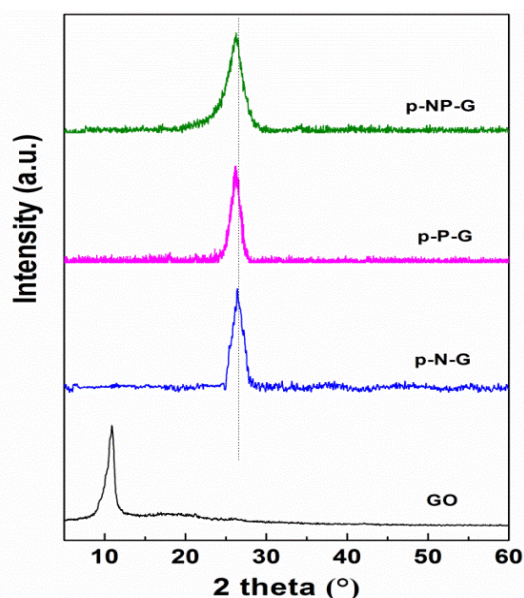

Fig. 1 XRD diffractograms of p-NP-G, p-N-G, p-P-G and GO.

XPS analysis was conducted to determine the doping levels and the bonding configuration of N and P in the doped graphene samples. As shown in Figure 2, the peaks at approximately 131 eV corresponded to P *2p* are observed for the p-NP-G and p-P-G samples[25, 31, 44]; and the peaks at 401 eV corresponded to N *1s* are observed in the p-NP-G and p-N-G samples[27, 30, 32]. These results indicate that both N and P atoms have been doped into the graphene successfully, and the doping levels of P and N in the p-N and P-G are 4.38% and 1.93%, respectively, as illustrated in Table S1. The fine split peaks of phosphorus in the high resolution P *2p* spectra (Fig S2a, c) reveal that P is covalently bonded with C and O to form the C–P (130.4 eV) and P–O bonds (132.8 eV)[27, 30]. The fine spilt peaks of nitrogen in the high-resolution N *1s* spectra (Fig S2b, d) demonstrate the graphitic N (401.2 eV), pyrrolic N (400.1 eV) and pyridinic N (398.4 eV) atoms in the N doped graphene[30, 35].
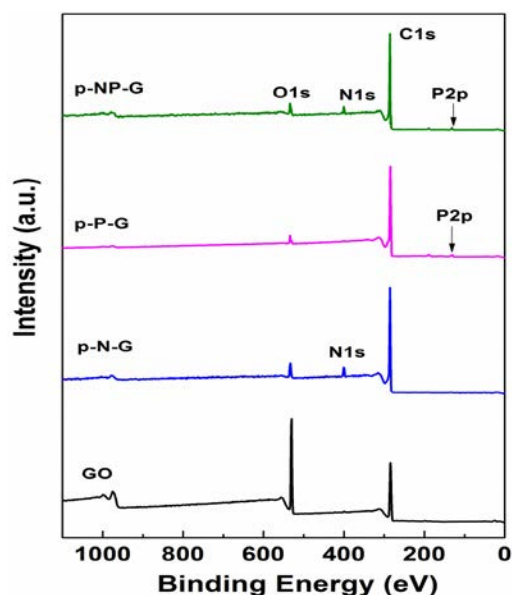

Fig. 2 XPS survey spectra of p-NP-G, p-N-G, p-P-G and GO.

In addition, Raman spectroscopy was employed to detect the density of defects in the graphene. The D band at 1350 cm^{-1} corresponds to the structural defects and disorders in the carbon matrix. The G band at approximately 1570 cm^{-1} is related to the E_{2g} vibration mode of the sp^2-bonded carbon atoms[35]. The intensity ratio of D band and G band (I_D/I_G) represents the disorder degree of graphene[30, 35]. As illustrated in Fig. 3, the p-NP-G sample occupies the highest value of I_D/I_G (1.31), followed by the p-P-G (1.23), p-N-G (1.16) and GO (1.05). This implies the N and P dual doped graphene contains more defects compared to the single P doped or N doped graphene[30]. Meanwhile, compared to the I_D/I_G values of p-P-G and p-N-G, it can be draw a conclusion that the P doing can result in more defects compared to the N doping even the P doping content (ca. 1.85%) is far less than that of N doping (ca. 4.54%)[30], and the more defects facilitates the heteroatoms doping in turn, which the heteroatoms doping can effectively contributes to the conductivity improvement of the graphene[31]. More importantly, the superior conductivity is one of the most important factors for a satisfactory polysulfides blocking

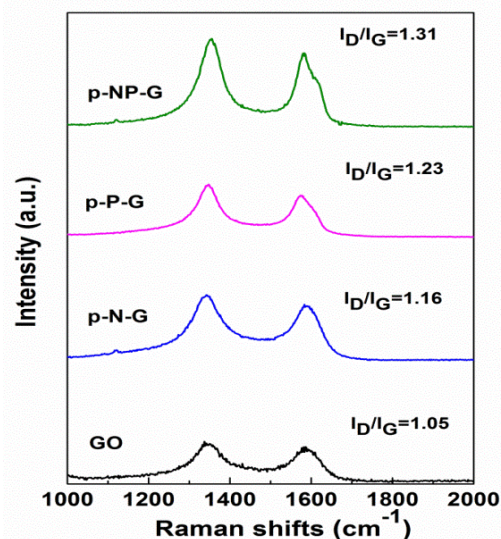layer as well as enhance the active materials utilization percentage[11, 45, 46].

Fig. 3 Raman spectra of p-NP-G, p-N-G, p-P-G and GO.

Note that the abundant porous structure is another key feature for the high quality blocking layer, as it physically accommodates the active materials S and polysulfides and facilitates electrolyte infiltration[6, 7, 33, 45].
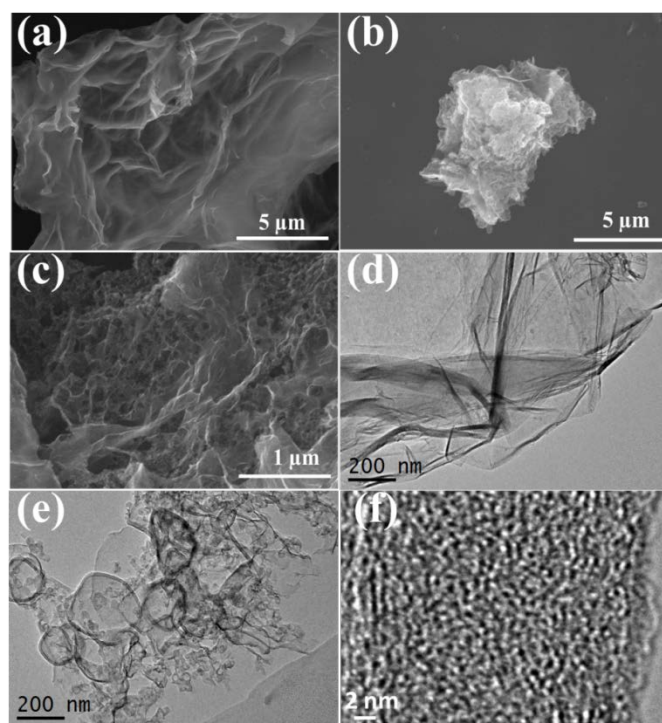

Fig. 4 SEM images of GO (a), p-NP-G (b) and (c);TEM images of GO (d), p-NP-G (e) and (f).

Therefore, the SEM and TEM characterizations were employed to investigate their microscopic structures. As shown in Figure 4a, the GO shows large-sized sheet structure. While the sheets of

the p-NP-G (Figure 4b and Figure 4c), p-N-G (Figure S3a) and p-P-G (Figure S3b), tend to aggregate and the sizes decrease, which is due to the decomposition of the oxygenous group of the GO in the annealing process. Furthermore, the p-NP-G and p-P-G samples illustrate the unique foam structures that are distinctive from that of the p-N-G sample, which may be due to the reaction of TPP and KOH at high temperature. Figure 4e and Figure S3d further demonstrate that the p-NP-G and p-P-G illustrate foam structures with a large amount of macropores with sizes range from tens of nanometers to hundreds of nanometers. However, the macropores are not observed for the GO and p-N-G samples from the TEM image as displayed in Figure 4d and Figure S3c. In addition, the high-resolution TEM image in Figure 4f confirms plenty of micropores in the p-NP-G sample, which agrees well with the N_2 adsorption/desorption results in Figure 5.

The N_2 adsorption/desorption was employed to further assess the textural properties of the samples. As shown in Figure 5, the p-NP-G and p-P-G samples exhibit the similar isotherm shapes (inset of Figure 5) which are combination of type I and type IV isotherms; while the N_2 adsorption/desorption isotherms of p-N-G and GO are attributed to the type I. This means the p-NP-G and p-P-G materials contain both the micropores and mesopores, while the micropores are dominant in the p-N-G and GO samples. It was further confirmed by the pore size distributions in Figure 5. In addition, from Table S2, it can be observed that the specific surface areas and pore volumes of the p-NP-G, p-P-G and p-N-G samples are nearly the same, but all far higher than that of the pristine GO, which is ascribed to the fact that the KOH can produce abundant micropores in the high temperature environment[6, 17]. The extra mesopores in the p-P-G and p-NP-G materials may be originated from the decomposition of TPP with the presence of KOH at high temperature. As mentioned above, these abundant pores not only greatly contribute to the electrolyte infiltration and polysulfides adsorption, which improve the active materials utilization and cycling performance[6, 45], but also accommodate significant volume change during the charge/discharge processes[45, 47].
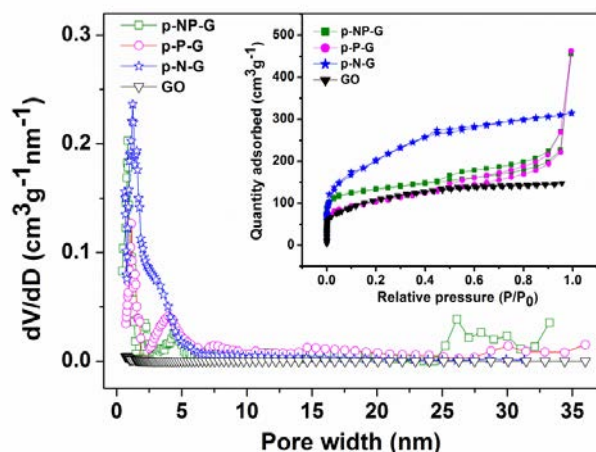

Fig. 5 N_2 adsorption/desorption isotherm plot and pore size distribution of p-NP-G, p-N-G, p-P-G and GO.

Density functional theory (DFT) calculation

The observation from materials characterizations suggest that the P doping may not only efficiently improve the conductivity, but also creates porous structure that might provide large surface area and pore volume to accommodate sulfur and polysulfides, which is beneficial for electrochemical performances of Li–S batteries.

Chemical adsorption could also play an important role in retaining sulfur and polysulfides and prohibiting the shuttling effect[5, 14, 48]. Recently it is reported that the chemical adsorption offered by the doped N on graphene could remarkably alleviate the polysulfides shuttling effect and achieve longevity of Li–S batteries[22, 32-35]. However, there is still no theoretical investigation on the adsorption behaviour of polysulfides on different reaction sites on multi-heteroatoms doped graphene, including the doped P, N atoms and –P–O function groups. Thus the first-principle DFT calculations on the adsorption behaviours of polysulfides in our work have been conducted.

Table 1 The calculated adsorption energies (E_{ads}) on different active sites of the surface of p-NP-G

Active sites	Graphitic N	Pyridinic N	Pyrrolic N	P	-P-O
E_{ads} (eV)	–0.567	–0.839	–1.138	–0.940	–1.390

To simplify the calculation, we employed the Li_2S_8 as the probe molecule to investigate the interaction configurations and energetics on the different adsorption sites. The calculated adsorption energies on different active sites of the p-NP-G are calculated and listed in Table 1 and the operated adsorption structure are listed in Fig. S4. Apparently, the larger adsorption energy reflects stronger adsorption capability. As shown in table 1, it can be observed the pyrrolic N shows strongest adsorption to Li_2S_8 among the three types of N, which is in line with the previous report[30]. Nevertheless, the –P–O affords even stronger adsorption to the sulphides than the pyrrolic N in that. The calculation results also demonstrate P atom has stronger adsorption capability to Li_2S_8 compared to graphitic N and pyridinic N in that P–O has the higher adsorption energy (–1.390). That may be due to, compared with N and C, atom P has a relatively larger atom radius. When P is doped in graphene, the larger atomic radius induces the longer bond distance between P and C atoms, which decreases the overlap of the p_z orbitals and decreases the π bonding[49]. Thus a considerable buckling of 1.28 Å appears in the vertical direction (see Figure S4d). The orbital hybridization of the P-doped region exhibits the features of sp^2 and sp^3 [50]. It is well-known that the pure graphene does not offer strong adsorption force to other groups species because of the sp^2 bonding, while the buckled graphene with partially sp^3 bonding could enhance the interaction between the graphene and other groups[51, 52]. When it comes to top –P–O functional group, the puckering and polarization becomes even larger than the pure P-doping one, which increases the interaction between Li_2S_8 and the graphene. In all, because of the different orbital hybridization and functional group, the doped P in graphene exhibits the relatively larger adsorption energy to Li_2S_8 than doped N in the graphene. Furthermore, compared with the single P-doped graphene sample, the doped N in the p-NP-G sample could provide additional adsorption sites for polysulfides. Therefore, the p-NP-G

sample shall offer the best adsorption capabilities among all the doped samples according to the DFT calculation.

Electrochemical evaluation

The $I-V$ curves of the tablets containing the same amount of as-prepared doped graphene materials are obtained in Figure 6. The straight line of the p-NP-G sample shows a typical Ohm resistant behavior. In the $I-V$ plot, the slope of the $I-V$ curve represents the relative conductivity of each sample. Therefore, the p-NP-G sample has the highest conductivity among all the samples [30], followed by the p-P-G and p-N-G samples, which indicates that N and P dual doping can significantly promote the electronic conductivity of graphene[30]. And the conductivity of the p-P-G (with a P concentration of ca. 1.85%) is higher than that of the p-N-G (with a N concentration of ca. 4.54%), implying that the contribution of P to the enhancement of the electronic conductivity is higher than that of N[30].
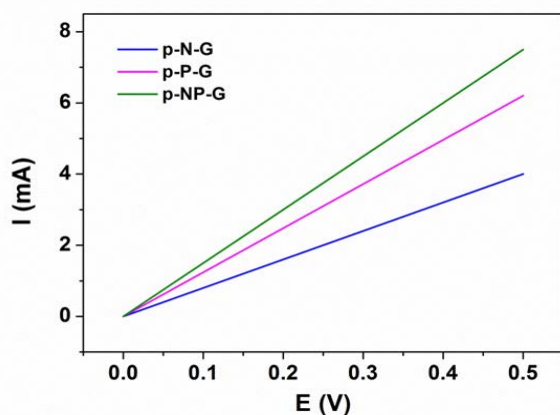

Fig. 6 $I-V$ curves of the as-prepared porous doped graphene samples.

The CV was conducted to reveal the electrochemical reaction mechanism of the cells with the interlayers. The CV curves of the first three cycles were measured between 1.5 and 3.0 V at a sweep rate of 0.1 mV/s as shown in Figure 7 a–c. Two main reduction peaks around 2.25 V and 2.05 V are observed during the cathodic scan, which correspond to the reduction of the elemental sulfur to the higher order lithium polysulfides (Li_2S_x, $4 \leqslant x \leqslant 8$), and the reduction of the higher order lithium polysulfides to the lower order lithium polysulfides, even to the insoluble Li_2S_2 and Li_2S, respectively[6, 45]. In the oxidation process, only one sharp oxidation peak is observed at approximately 2.35–2.40 V in Figure 7b–c, corresponding to the transformation of Li_2S_2 and Li_2S into the polysulfides[6, 45]. The peaks in Figure 7c remain almost identical from the first three cycles, demonstrating the good cycling stability of the sulfur electrode with the p-NP-G interlayer. In addition, it can be observed that the peak position difference between the reduction peak and the oxidation peak of the p-NP-G interlayer is the smallest. Meanwhile, the oxidation peak potentials in Figure 7 a–b are more positive and the peak widths are larger compared to that in Figure 7c. These observations suggest that the p-NP-G sample has the smallest polarization due to the highest conductivity.[6, 21]
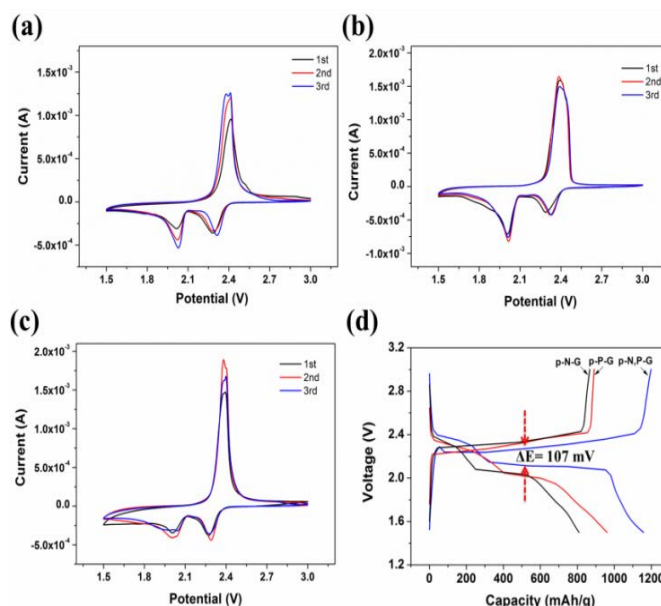

Fig.7 CV curves of the cell with p-N-G (a), p-P-G (b), p-NP-G (c) and Galvanostatic charge/discharge profiles of p-NP-G, p-N-G and p-P-G (d).

The initial galvanostatic charge/discharge behaviors of the Li–S batteries were evaluated at the current density of 1 C as shown in Figure 7d. The cells with the interlayers consist of two plateaus that correspond to the reduction of the elemental sulfur to the soluble polysulfides at around 2.3 V and to the insoluble Li_2S_2/Li_2S at approximately 2.1 V[6, 21, 45], respectively. In particular, p-NP-G interlayer possess the widest plateaus and most stable with a relatively low polarization of 107 mV (*vs.* 249 mV for p-N-G and 221 mV for p-P-G) at 1 C, which suggests a kinetically more efficient reaction process with a smaller barrier[21, 53, 54]. Furthermore, The charge/discharge plateaus obviously decrease in the cell with the single doped graphene interlayer, which indicates the high polarization and slow redox reaction kinetics with the inferior reversibility[21]. The superior properties of the cell with the p-NP-G interlayer can be ascribed to its excellent electrical conductivity and the abundant porous structure, which promotes the reaction kinetics of the cathode. It's worth mentioning that the results are consistent well with the CV measurements.

The cycling performances of the cells with the interlayers are tested in a current density of 1 C between 1.5 V and 3.0 V and illustrated in Figure 8a. As expected, the cells with the p-NP-G interlayer reveals the highest initial capacity with 1158.3 mAh/g, followed by the cells with the p-P-G (962.8 mAh/g) and p-N-G (867.1 mAh/g) interlayers, respectively. There is an increase of the capacity in the initial dozens of cycles, suggesting the presence of a stabilization and activation process, which is likely attributed to the re-distribution of the active materials on the interlayer surface[35, 55]. More importantly, the cells with the p-NP-G interlayer still shows a high reversible capacity of 638.0 mAh/g even after 500 cycles, but the cells with the p-P-G and p-N-G interlayers show lower reversible capacity of 481.7 and 322.3 mAh/g, respectively. In addition, the coulombic efficiencies of the cells with the p-NP-G interlayers are nearly 100%, indicating that

the sulfur shuttle phenomenon was effectively restricted to a lower level[33].

The rate capabilities of the cells with the interlayers at various C-rates from 0.2 C to 2 C are displayed in Figure 8b. After activated at the low (0.2 C) and middle (0.5 C) current densities, all cells can retain the relative stable capacity at the high current densities (1 C–2 C). Note that the cell with the p-NP-G interlayer presents the highest capacity among the cells no matter at low or high current densities. Even the charge/discharge current densities increased to 2 C, the cell with the p-NP-G interlayer can still remain an outstanding reversible capacity of 633.7 mAh/g, in comparison with 507.8 and 402.3 mAh/g for the cells with the p-P-G and P-N-G interlayers, respectively. When the current returns back to 0.5 C, the capacity of the cell with p-NP-G interlayer recovers to 858.9 mAh/g, indicating a fairly stable structure of the sulfur cathode in the cell[34, 45].
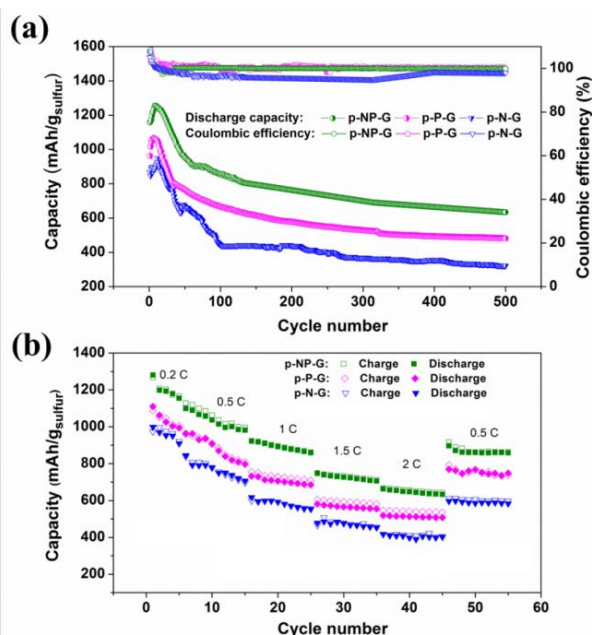

Fig.8 (a) Cycle life of the cells with heteroatom doped graphene interlayers at 1 C and (b) Rate capability of the cells with heteroatom doped graphene interlayers.

The EIS measurements were conducted to gain additional insights about the effects of N and P doping. The Nyquist plots of the cells with all types of the interlayers before cycling and after 100 cycles are modelled with the equivalent circuit and shown in Figure 9. Before cycling, the Nyquist plots for these electrodes consist of a single depressed semicircle in the high-to-medium frequency region and an inclined line in the low frequency region (Figure 9a), which correspond to the charge-transfer resistance R_{ct} and the Warburg impedance (W_0)[6, 21, 45], respectively. The high-frequency intercept on the real axis represents the ohmic resistance (R_e) of the cell, including the electrolyte and electrode resistances[6, 45]. Two semicircles (Figure 9b) can be observed from the Nyquist plot of the cells after 100 cycles. The semicircle in the high-frequency region reflects a passivation film that is contributed by the Li_2S (or Li_2S_2) layers on the surface of the electrode[3, 21], while the semicircle in the medium-frequency range is related to the resistance (R_{ct}) of the

interfacial charge transfer process[3, 21]. The R_e, R_s, R_{ct} values of the cells with different interlayers acquired from the equivalent circuits are shown in Table S3. Before cycling, the R_{ct} value of p-P-G (44.24 Ω) is far less than p-N-G (160.7 Ω), demonstrating the p-P-G has higher conductivity than the p-N-G, consistent with the results from $I-V$ curves. And the R_{ct} value of the p-NP-G (24.87 Ω) interlayer is the lowest, which may results from N and P dual doped. After 100 cycles, the R_{ct} values of all the cells decrease remarkably when compared with that before cycling. This may be caused by the adequate infiltration of the electrolyte, chemical activation process for the dissolution and re-distribution of the active materials[45]. Furthermore, the R_s value for the cell with the p-NP-G (7.53 Ω) interlayer is much lower than those with the p-P-G (23.92 Ω) and p-N-G (28.51 Ω) interlayers, which indicates that the p-NP-G interlayer can more efficiently prevent the polysulfides from shuttling to the anode[21, 45] and that N, P dual doping can co-functionalize on improving the electrochemical performances of the Li–S batteries compared to the single doped graphene. Simultaneously, that the R_s value of p-P-G is smaller than p-N-G verifies the P doing is more beneficial to adsorbing the polysulfides compared to the N doping, agreeing well with the observation in physical conductivity measurements Figure 6 and the DFT calculation results.
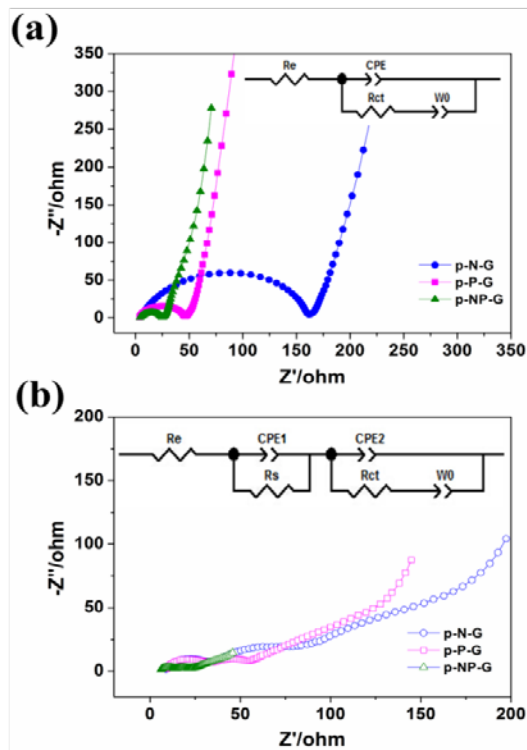

Fig. 9 The Nyquist plots (a) before discharge and (b) after 100 cycles of the Li–S cells with various interlayers and equivalent circuit models (inset of Fig. 9a and Fig. 9b).

Conclusions

The porous nitrogen and phosphorus dual doped graphene (p-NP-G) has been successfully synthesized via an annealing

and hydrothermal method and been employed as the polysulfides blocking layer for Li–S batteries. The materials characterizations and DFT first principle calculation suggest that the N and P dual doping process to graphene can not only effectively improve the electronic conductivity of the graphene framework, but also provide strong adsorption force to polysulfides and effectively tackle the shuttling effect of polysulfide. Meanwhile, the abundant micropores formed by the p-NP-G physically confine polysulfides and facilitate the electrolyte infiltration. As a result of all these factors, the battery cells with the p-NP-G interlayer demonstrate the prominent electrochemical performances with a superior high initial capacity(1158.3 mA h/g at the current density of 1 C), excellent rate capability (633.7 mA h/g at 2 C), and satisfactory cycling stability (ca. 0.09% capacity decay per cycle). This work also suggests that designing the porous and conductive graphene as a blocking layer via dual N, P doping can be a very promising strategy for manufacturing high performance Li–S batteries.

Acknowledgements

Notes and references

[a] Centre for Clean Environment and Energy, Environmental Futures Insititute, Griffith School of Environment, Gold Coast Campus, Griffith University QLD 4222, Australia. Fax: 61-755047588; Tel: 61-7-55528155; E-mail: s.zhang@griffith.edu.au

[b] Department of Materials Science and Engineering, College of Engineering, Peking University, Beijing 100871, China. E-mail: hou@pku.edu.cn

[c] Beijing Computational Science Research Centre, Beijing 100871, China. Email: limin.liu@csrc.ac.cn

† Footnotes should appear here. These might include comments relevant to but not central to the matter under discussion, limited experimental and spectral data, and crystallographic data.

Electronic Supplementary Information (ESI) available: [details of any supplementary information available should be included here]. See DOI: 10.1039/b000000x/

1. J. Q. Huang, X. F. Liu, Q. Zhang, C. M. Chen, M. Q. Zhao, S. M. Zhang, W. c. Zhu, W. Z. Qian and F. Wei, *Nano Energy*, 2013, **2**, 314–321.

2. K. Xi, B. Chen, H. Li, R. Xie, C. Gao, C. Zhang, R. V. Kumar and J. Robertson, *Nano Energy*, 2015, **12**, 538–546.

3. S. Y. Zheng, Y. Wen, Y. J. Zhu, Z. Han, J. Wang, J. H. Yang and C. S. Wang, *Adv. Energy Mater.*, 2014, **4**, Doi 10.1002/Aenm.201400482.

4. K. Xi, S. Cao, X. Peng, C. Ducati, R. V. Kumar and A. K. Cheetham, *Chem Commun (Camb)*, 2013, **49**, 2192–2194.

5. Z. Wang, Y. Dong, H. Li, Z. Zhao, H. B. Wu, C. Hao, S. Liu, J. Qiu and X. W. Lou, *Nat Commun*, 2014, **5**, 5002–5009.

6. X. Gu, Y. Wang, C. Lai, J. Qiu, S. Li, Y. Hou, W. Martens, N. Mahmood and S. Zhang, *Nano Res.*, 2015, **8**, 129–139.

7. C. Xu, Y. Wu, X. Zhao, X. Wang, G. Du, J. Zhang and J. Tu, *J. Power Sources*, 2015, **275**, 22–25.

8. D. W. Wang, G. Zhou, F. Li, K. H. Wu, G. Q. Lu, H. M. Cheng and I. R. Gentle, *Phys. Chem. Chem. Phys.*, 2012, **14**, 8703–8710.

9. Q. C. Zeng, F. Li, I. R. Gentle, H.-M. Cheng and D.-W. Wang, *Carbon*, 2015, **93**, 161–168.

10. Y. S. Su and A. Manthiram, *Nat. Commun.*, 2012, **3**, 1166–1171.

11. Y. S. Su and A. Manthiram, *Chem. Commun.*, 2012, **48**, 8817–8819.

12. S. H. Chung and A. Manthiram, *Adv. Mater.*, 2014, **26**, 1360–1365.

13. S. H. Chung and A. Manthiram, *Chem. Commun.*, 2014, **50**, 4184–4187.

14. H. Yao, K. Yan, W. Li, G. Zheng, D. Kong, Z. W. Seh, V. K. Narasimhan, Z. Liang and Y. Cui, *Energy Environ. Sci.*, 2014, **7**, 3381–3390.

15. Y. Chen, J. Zhu, B. Qu, B. Lu and Z. Xu, *Nano Energy*, 2014, **3**, 88–94.

16. Q. Liu, Z. F. Li, Y. Liu, H. Zhang, Y. Ren, C. J. Sun, W. Lu, Y. Zhou, L. Stanciu, E. A. Stach and J. Xie, *Nat. Commun.*, 2015, **6**, 6127–6137.

17. Y. Huang, D. Wu, J. Jiang, Y. Mai, F. Zhang, H. Pan and X. Feng, *Nano Energy*, 2015, **12**, 287–295.

18. F.-Y. Su, Y.-B. He, B. Li, X.-C. Chen, C.-H. You, W. Wei, W. Lv, Q.-H. Yang and F. Kang, *Nano Energy*, 2012, **1**, 429–439.

19. D. Kong, H. He, Q. Song, B. Wang, W. Lv, Q.-H. Yang and L. Zhi, *Energy Environ. Sci.*, 2014, **7**, 3320–3325.

20. H. J. Peng, J. Y. Liang, L. Zhu, J. Q. Huang, X. B. Cheng, X. F. Guo, W. P. Ding, W. C. Zhu and Q. Zhang, *ACS Nano*, 2014, **8**, 11280–11289.

21. G. Zhou, S. Pei, L. Li, D. W. Wang, S. Wang, K. Huang, L. C. Yin, F. Li and H. M. Cheng, *Adv. Mater.*, 2014, **26**, 625–631.

22. M. Q. Zhao, Q. Zhang, J. Q. Huang, G. L. Tian, J. Q. Nie, H. J. Peng and F. Wei, *Nat. Commun.*, 2014, **5**, 3410–3417.

23. C. Zhang, D. H. Liu, W. Lv, D. W. Wang, W. Wei, G. M. Zhou, S. Wang, F. Li, B. H. Li, F. Kang and Q. H. Yang, *Nanoscale*, 2015, **7**, 5592–5597.

24. N. Mahmood, C. Zhang and Y. Hou, *Small*, 2013, **9**, 1321–1328.

25. N. Mahmood, C. Z. Zhang, F. Liu, J. H. Zhu and Y. L. Hou, *ACS Nano*, 2013, **7**, 10307–10318.

26. C. Zhang, R. Hao, H. Liao and Y. Hou, *Nano Energy*, 2013, **2**, 88–97.

27. C. Zhang, N. Mahmood, H. Yin, F. Liu and Y. Hou, *Adv. Mater.*, 2013, **25**, 4932-4937.

28. H. Yin, C. Zhang, F. Liu and Y. Hou, *Adv. Funct. Mater.*, 2014, **24**, 2930–2937.

29. Z. Yang, Z. Yao, G. F. Li, G. Y. Fang, H. G. Nie, Z. Liu, X. M. Zhou, X. A. Chen and S. M. Huang, *ACS Nano*, 2012, **6**, 205–211.

30. X. Ma, G. Ning, C. Qi, C. Xu and J. Gao, *ACS Appl. Mater. Interfaces*, 2014, **6**, 14415–14422.

31. Z. S. Wu, W. C. Ren, L. Xu, F. Li and H. M. Cheng, *ACS Nano*, 2011, **5**, 5463–5471.

32. Y. Qiu, W. Li, W. Zhao, G. Li, Y. Hou, M. Liu, L. Zhou, F. Ye, H. Li, Z. Wei, S. Yang, W. Duan, Y. Ye, J. Guo and Y. Zhang, *Nano Lett.*, 2014, **14**, 4821–4827.

33. C. Wang, K. Su, W. Wan, H. Guo, H. Zhou, J. Chen, X. Zhang and Y. Huang, *J. Mater. Chem. A*, 2014, **2**, 5018–5023.

34. X. Wang, Z. Zhang, Y. Qu, Y. Lai and J. Li, *J. Power Sources*, 2014, **256**, 361–368.

35. K. Han, J. Shen, S. Hao, H. Ye, C. Wolverton, M. C. Kung and H. H. Kung, *ChemSusChem*, 2014, **7**, 2545-2553.

36. L. J. Cote, F. Kim and J. Huang, *J. Am. Chem. Soc.*, 2009, **131**, 1043–1049.

37. G. Kresse, *Phys. Rev. B*, 1996, **54**, 11169–11186.

38. P. E. Blochl, *Phys. Rev. B*, 1994, **50**, 17953–17979.

39. G. Kresse, *Phys. Rev. B*, 1999, **59**, 1758–1775.

40. J. P. Perdew, K. Burke and M. Ernzerhof, *Phys. Rev. Lett.*, 1996, **77**, 3865–3868.

41. L. M. Liu, R. Car, A. Selloni, D. M. Dabbs, I. A. Aksay and R. A. Yetter, *J. Am. Chem. Soc.*, 2012, **134**, 19011–19016.

42. S. Grimme, J. Antony, S. Ehrlich and H. Krieg, *J. Chem. Phys.*, 2010, **132**, 154104−154123.

43. W. Chen, L. Yan and P. R. Bangal, *Carbon*, 2010, **48**, 1146–1152.

44. G. M. Zhou, L. C. Yin, D. W. Wang, L. Li, S. F. Pei, I. R. Gentle, F. Li and H. M. Cheng, *ACS Nano*, 2013, **7**, 5367–5375.

45. X. Gu, C. Lai, F. Liu, W. Yang, Y. Hou and S. Zhang, *J. Mater. Chem. A*, 2015, **3**, 9502–9509.

46. J. Song, Z. Yu, T. Xu, S. Chen, H. Sohn, M. Regula and D. Wang, *J. Mater. Chem. A*, 2014, **2**, 8623–8627.

47. S. H. Chung and A. Manthiram, *J. Phys. Chem. Lett.*, 2014, **5**, 1978–1983.

48. Q. Li, C. Zhou, Z. Ji, B. Han, L. Feng and J. Wu, *J. Mater. Chem. A*, 2015, **3**, 7241–7247.

49. C.-J. Tong, H. Zhang, Y.-N. Zhang, H. Liu and L.-M. Liu, *J. Mater. Chem. A*, 2014, **2**, 17971–17978.

50. H. L. Zhuang, A. K. Singh and R. G. Hennig, *Phys. Rev. B*, 2013, **87**, 165415–165422.

51. Yang Zhi , Yao Zhen, Li Guifa , Fang Guoyong, Nie Huagui, Liu Zheng, Zhou Xuemei, C. Xi'an and H. Shaoming, *ACS Nano*, 2012, **6**, 205–211.

52. Q. Zhang, Y. Wang, Z. W. Seh, Z. Fu, R. Zhang and Y. Cui, *Nano Lett*, 2015, DOI: 10.1021/acs.nanolett.5b00367..

53. G. Zheng, Y. Yang, J. J. Cha, S. S. Hong and Y. Cui, *Nano Lett.*, 2011, **11**, 4462–4467.

54. X. Yang, L. Zhang, F. Zhang, Y. Huang and Y. Chen, *ACS Nano*, 2014, **8**, 5208–5215.

55. S. S. Zhang and J. A. Read, *J. Power Sources*, 2012, **200**, 77–82.